BJRS

BRAZILIAN JOURNAL
OF
RADIATION SCIENCES
10-03A (2022) 01-18

CFD analysis of a wire-wrapped infinite sub-channel using temperature-dependent LBE properties

Umezu[a] I.K., Costa[a] A.L., Godino[b] D.M., Santos[c] A.A.C.

[a] *Departamento de Engenharia Nuclear - DEN, Universidade Federal de Minas Gerais - UFMG, Av. Pres. Antônio Carlos, 6627, Pampulha, 31270-901, Belo Horizonte - MG, Brazil. ivkeum@ufmg.br.*

[b] *CIMEC Centro de Investigación de Métodos Computacionales, UNL, CONICET, FICH, Col. Ruta 168 s/n, Predio Conicet "Dr. Alberto Cassano", 3000 Santa Fe, Argentina.*

[c] *Centro de Desenvolvimento de Tecnologia Nuclear – Comissão Nacional de Energia Nuclear Av. Pres. Antônio Carlos, 6627, Pampulha, 31270-901, Belo Horizonte - MG, Brazil*

ABSTRACT

Once a significant number of LMFRs (liquid-metal cooled fast nuclear reactors) employ wire-wrapped fuel assemblies, considerable attention should be directed to this engineering feature. Given the many contact points and tight gaps, wire-wrapped fuel assemblies are difficult to analyze without numerical tools, out of which CFD (computational fluid dynamic) is the leading tool in the field. This work presents a CFD analysis of a wire-wrapped infinite sub-channel, based on MYRRHA's fuel assembly geometry and with LBE (lead bismuth eutectic) coolant properties implemented as temperature-dependent polynomial curves. Periodic boundary conditions were applied, and the turbulence model chosen was k-ω SST. All calculations were run on ANSYS Fluent R19.3. Following good engineering practices for CFD simulations, a GCI (grid convergence index) analysis was carried out, in order to ensure grid/mesh independence on the results. Ultimately, the main goal of this work was to evaluate if the implementation of temperature-dependent thermal-physical properties for LBE coolant would lead to any different results, when compared to the static properties. However, no significant result change was observed in this case, only an increase in computational time, which leads to the conclusion that for small domains with periodic boundaries, the implementation of temperature-dependent coolant properties is not justifiable.

Keywords: **Wire-wrapped; CFD; GCI; LBE.**

ISSN: 2319-0612
DOI: https://doi.org/10.15392/2319-0612.2022.1949
Submitted: 2022-01-31
Accepted: 2022-11-27

1. INTRODUCTION

In the new context of Generation IV technologies [1], liquid metal cooled fast reactors (LMFR) are in a promising position, given their inherent safety, nuclear waste reduction and fuel consumption sustainability. One of the most distinguishing engineering features of LMFR is the employment of wire-wrapped fuel assemblies, which consist in metal wires revolved around the fuel rods, making it a compact and stiff assembly. However, due to the large amount of contact points and tight gaps, wire-wrapped fuel assemblies are considered to be complex in geometry, which makes analytical predictions practically impossible and highlights the importance of a consistent Computational Fluid Dynamics (CFD) modeling approach, such as developed in recent years by [4-7].

In this work, an infinite wire-wrapped fuel assembly CFD analysis is carried out evaluating the results for stream-wise velocity, fluid temperature and turbulent kinetic energy. The geometry was based on the current fuel assembly design of the MYRRHA project [3] and temperature-dependent LBE thermal-physical properties [2] were employed, like in [10]'s work.

Given that most works on CFD simulations of MYRRHA's infinite wire-wrapped sub-channels [5-7] were only done using fixed thermal-physical coolant properties (density, dynamic viscosity, thermal conductivity and specific heat), this work's main goal is to bring a brief evaluation of whether the implementation of variable coolant properties leads to different results on the velocity, temperature and turbulent kinetic energy fields, when compared to the use of static properties.

To ensure that the modelling approach for this work is adequate, three evaluations were carried out. The first, to check the mesh convergence and independence on results, applied the GCI (grid convergence index) method, following the procedures presented by [9]. The second, using fixed thermal-physical properties, compared this work's initial results for the k-ω turbulence model to the work of [6], in which various RANS (Reynold Averaged Navier-Stokes) simulations were compared to a high-fidelity quasi-Direct Numeric Simulation (q-DNS) [5]. The third and last evaluation, the main aim of this work, is to compare the quantitative results and computational costs from simulations using constant and variable thermal-physical LBE properties.

2. MATERIALS AND METHODS

2.1. Analysis Domain and Boundary Conditions

With the intentions of comparing results, the infinite wire-wrapped computational domain used in this work is the same as the one used in the works by [5] and [6], all based on the current MYRRHA design, detailed in Table I. The infinite domain consists of a sub-channel with one central rod and 6 surrounding rods, with a length equal to one wire-wrap pitch, thus making it possible to be modeled with periodic boundary conditions in 3 radial and in the axial directions.

Figure 1 (a) presents the geometrical representation of the sub-channel, an extracted volume between wire-wrapped fuel rods. The use of an infinite domain is justified by the computational unviability of simulating a whole MYRRHA fuel assembly, which is made up of 127 wire-wrapped fuel pins [3]. Also, the infinite domain analysis provides valuable information regarding flow patterns and temperature distributions along the sub-channel, which tends to repeat itself along the whole assembly, except for the sub-channels adjacent to the assembly wrapper walls. Figure 1 (b) shows the domain's cross section with the evaluation lines.

The coolant employed in this analysis is Lead-Bismuth Eutectic (LBE), modelled with temperature dependent properties, as presented in Table III. The constant properties for LBE at 340 ºC (the inlet temperature used by [5]) is presented in Table II. The percentual differences between the two approaches for 340 ºC is presented in Table IV. As for the thermal boundary conditions, a constant heat flux of Q = 152 kW/m² is applied to the fuel rod walls, and the wires are modelled as adiabatic walls, the same conditions used by [5] and [6].

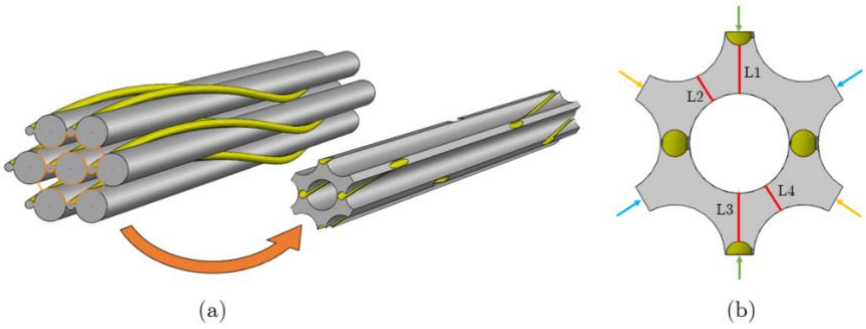

Figure 1: *(a) Infinite wire-wrapped sub-channel extracted volume. (b) Sub-channel cross section.*
Source: Authors

Table I: Dimensions of the infinite wire-wrapped assembly [5].

Dimensions	**Value**
Rod diameter (D) [mm]	6.55
Wire diameter [mm]	1.75
Wire wrapping pitch [mm]	262
Gap between rod and wire [mm]	0.1

Table II: Thermal-physical LBE properties at 340 ºC [5].

Thermal-physical property	**Value**
Density [kg·m^{-3}]	$\rho = 10285$
Thermal Conductivity [W·m^{-1}· K^{-1}]	$k = 12.25$
Dynamic Viscosity [Pa·s]	$\mu = 1.69 \times 10^{-3}$
Heat Capacity [J·kg^{-1}· K^{-1}]	$\mathrm{Cp} = 145$

Table III: Temperature dependent thermal-physical LBE properties.

Thermal-physical property	**Temperature Dependent Function (T in Kelvin)**
Density [kg·m^{-3}]	$\rho(T) = 11065 - 1.293 \cdot T$
Thermal Conductivity [W·m^{-1}· K^{-1}]	$k(T) = 3.284 + 0.01617 \cdot T - 2.305 \times 10^{-6} \cdot T^2$
Dynamic Viscosity [Pa·s]	$\mu(T) = 3.46 \times 10^{-3} - 2.888 \times 10^{-6} \cdot T$
Heat Capacity [J·kg^{-1}· K^{-1}]	$\mathrm{Cp}(T) = 156.23 - 0.0197 \cdot T$

Table IV: Difference for LBE constant and variable properties at 340 ºC.

Thermal-physical property	**Constant**	**Variable**	**Difference***
Density [kg·m^{-3}]	$\rho = 10285$	$\rho = 10272$	0.12 %
Thermal Conductivity [W·m^{-1}· K^{-1}]	$k = 12.25$	$k = 12.33$	0.67 %
Dynamic Viscosity [Pa·s]	$\mu = 1.690 \times 10^{-3}$	$\mu = 1.689 \times 10^{-3}$	0.05 %
Heat Capacity [J·kg^{-1}· K^{-1}]	$\mathrm{Cp} = 145$	$\mathrm{Cp} = 144.15$	0.58%

*Difference = |(Constant value – Variable value) / (Constant value)|x100%

The temperature dependent functions for density and thermal conductivity were directly extracted from [2]. Dynamic viscosity and heat capacity, also from [2], were adapted into linear functions. For the temperature range of 600 K and 700 K, the coefficients of determination (R^2) were 0.9926 and 0.9991, respectively.

Three translational periodic boundary conditions were applied to the opposite boundaries of the cross section, shown in Figure 1 (b) as matching color arrows, and one inlet-outlet periodic boundary condition, with a fixed mass flow rate of $\dot{m} = 1.4512\ kg/s$ was imposed, based on an average inlet velocity of 2 m/s and with fixed LBE density at 340 ºC, [8].

The calculations were run on Ansys Fluent® R19.3, employing the RANS-based linear k-ω SST turbulence model, due to its robustness, relatively low computational cost and, most importantly, due to its good predictions when studied by [6], where this model's results were compared to the results from a q-DNS simulation of the same infinite wire-wrapped subchannel. In order to improve convergence speed and computational costs, the simulations were calculated using Fluent's pressure-coupled based solver and, when possible, GPGPU acceleration capabilities were applied.

2.2. Grid/Mesh Refinement Process

Considering the high level of complexity in the regions between the wires and rods, and the k-ω model requirements for low y^+ values around non-slip walls [11], the mesh refinement was majorly focused on the fuel rod and wire walls. It is important to have mesh fine enough, but not too computationally expensive, in order to optimize the time consumed when comparing all the studied cases. The chosen method for this study was the GCI analysis, proposed by [9]. This method is described by the following set of equations, which determine the discretization error between the meshes used in this study. Although thoroughly described in [9], a brief presentation of the method is given below.

First, let h denote the representative cell size within a mesh, as defined in Equation 1:

$$h = \left| \frac{1}{N} \sum_{i=1}^{N} (\Delta V_i) \right|^{1/3} \quad (1)$$

where ΔV_i is the volume of each cell in a mesh of N elements. Given that $h_1 < h_2 < h_3$ and that r denotes the refinement ratio between successive meshes, r_{12} and r_{23} can be defined as $r_{12} = h_1/h_2$ and $r_{23} = h_2/h_3$. Moving on to the Equation 2, p gives the apparent order of accuracy, which can be determined using the fixed-point iteration method:

$$p = \frac{1}{l\,n(r_{12})} \left| ln \left| \frac{\varepsilon_{32}}{\varepsilon_{21}} \right| + ln \left(\frac{{r_{21}}^p - s}{{r_{32}}^p - s} \right) \right| \quad (2)$$

where $s = sign(\varepsilon_{32}/\varepsilon_{32})$, $\varepsilon_{32} = \phi_3 - \phi_2$, $\varepsilon_{21} = \phi_2 - \phi_1$, and ϕ_n is the quantity being evaluated in mesh n. The extrapolated values are calculated as:

$${\phi_{ext}}^{21} = (\phi_1 {r_{21}}^p - \phi_2)/({r_{21}}^p - 1) \quad (3)$$

with ${\phi_{ext}}^{32}$ being calculated in its equivalent way. Finally, the error estimates, the extrapolated error and the fine-grid convergence index are respectively presented by Equations 4, 5 and 6:

$${e_a}^{21} = \left| \frac{\phi_1 - \phi_2}{\phi_1} \right| \quad (4)$$

$${e_{ext}}^{21} = \left| \frac{{\phi_{ext}}^{21} - \phi_1}{{\phi_{ext}}^{21}} \right| \quad (5)$$

$$GCI_{21} = \frac{1.25 {e_a}^{21}}{{r_{21}}^p - 1} \quad (6)$$

Values for ${e_a}^{32}$, ${e_{ext}}^{32}$ and GCI_{32} are similarly calculated. Equation 6 will be the one used when plotting the discretization error along the fine grid solution. The calculations and graphical plots for the GCI were all run on a MATLAB® script.

Following the methodology above, three meshes were evaluated for nondimensionalized temperature (T^+) along line 1 (L1), Figure 1 (b). Mesh 1 with 14.20 million cells, Mesh 2 with 9.06 million and Mesh 3 with 6.10 million. Between every refinement process, a reduction of around 30% in size for all mesh size parameters were applied. Following the sensitivity analysis already performed by [6], 8 prism layers were considered for all three cases, with their first height equal to 0.01 mm. Figure 2 presents the visual differences among the three meshes around the wire-rod gap region.

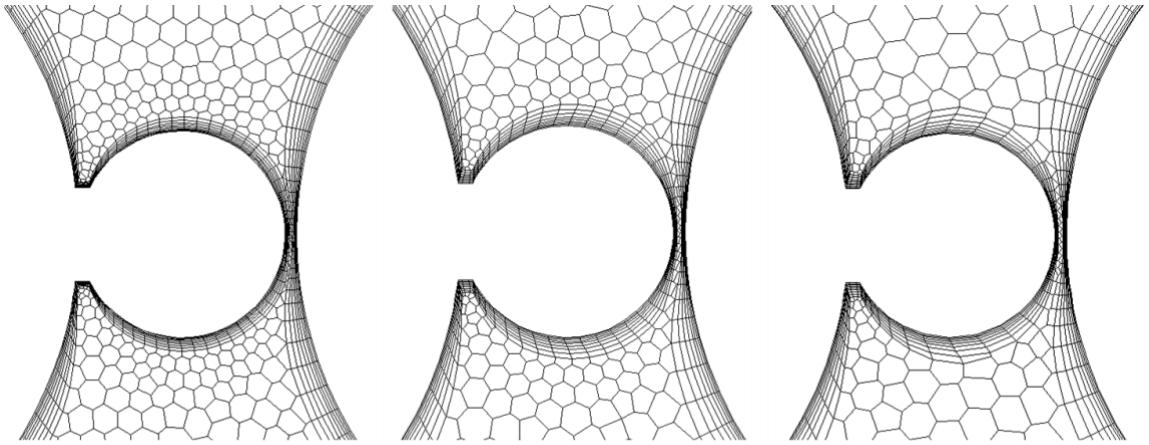

Figure 2: *Visual differences between meshes 1 (a), 2 (b) and 3 (c).*
Source: Authors

Applying the GCI analysis described above, the values for ϕ_n evaluated were the nondimensionalized temperature (T^+) along L1, as shown in Figure 3. As seen in Figure 4, the GCI discretization errors between meshes 1 and 2 all remained within 4%. Such results indicates that any refinements beyond mesh 2 do not improve the quality of the results. Thus, mesh 2 is the one employed in the following analyses.

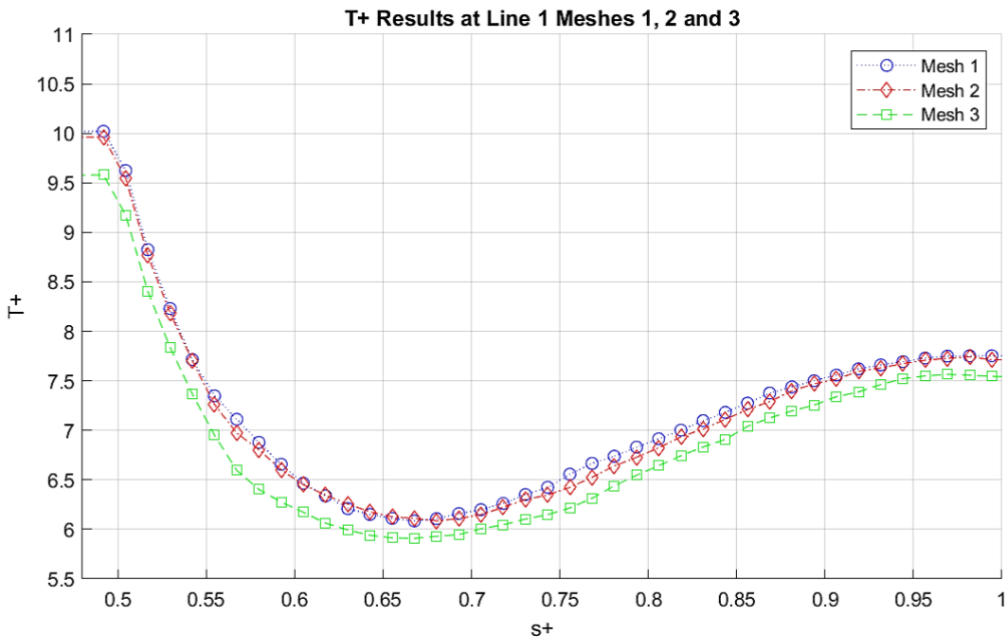

Figure 3: *Comparative results for T^+ values from meshes 1, 2 and 3 at L1.*
Source: Authors

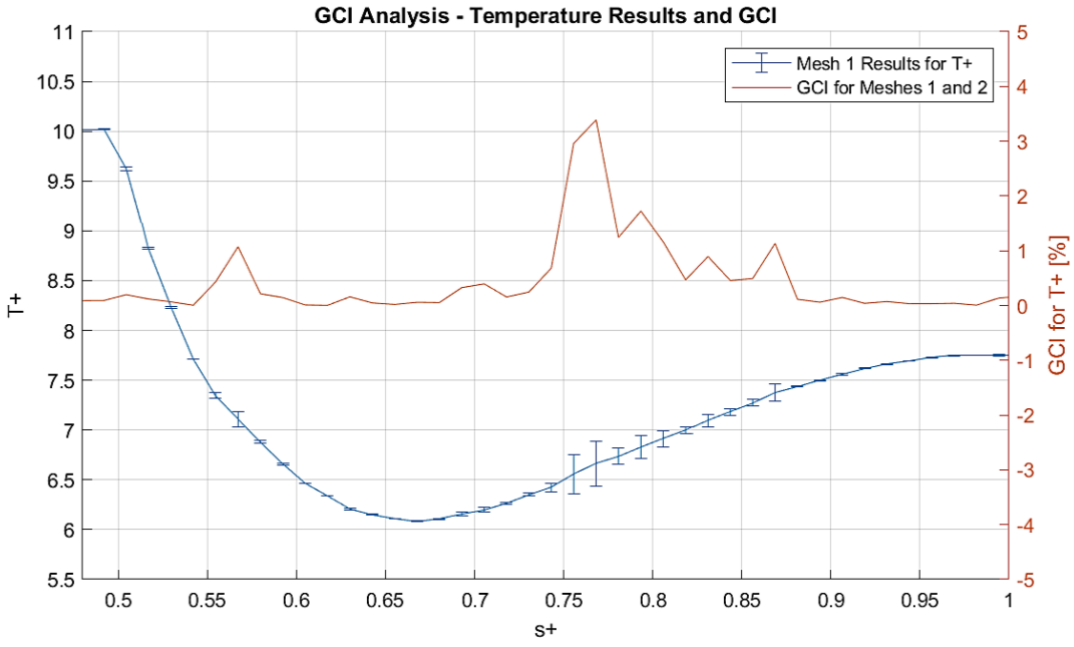

Figure 4: *Mesh 1 results for T^+ at L1 with GCI error bars.*
Source: Authors

3. RESULTS AND DISCUSSION

3.1. Qualitative comparison with validated k-ω SST results

Firstly, to allow a direct comparison between the results, the fields were non-dimensionalized using the average frictional velocity u_t [8]. The averaged axial velocity, temperature and turbulent kinetic energy fields are respectively defined by the following equations 7, 8 and 9:

$$W^+ = \frac{\mathrm{W}}{u_t} \tag{7}$$

$$T^+ = \frac{(\mathrm{T} - \mathrm{T_{min}}) \times (\rho \cdot C_p \cdot u_t)}{Q} \tag{8}$$

$$TKE^+ = \frac{TKE}{u_t^2} \tag{9}$$

For the qualitative comparison, mesh 2 results are presented alongside [6]'s results above mentioned fields in Figure 5. All contours are plotted on the domain's midplane, i.e., at longitudinal length equal to 131 mm. The contours (a), (c) and (e) are from [6], (b), (d) and (f) are this work's results using their own adjusted scale. This qualitative analysis is important in order to observe not the values themselves, but the field's distributions and general behavior. The numerical differences will be presented in the next section.

It can be observed that all of the three field distributions and general shapes are in accordance with [6]'s validated results for the k-ω SST simulations. However, in the gap region between the fuel rods and the wires, a considerable flow stagnation can be seen in [6]'s results, but not in this work's results. This difference can influence directly in the values of temperature, where the greatest numerical divergences are observed around the central rod, as it is presented in the following charts.

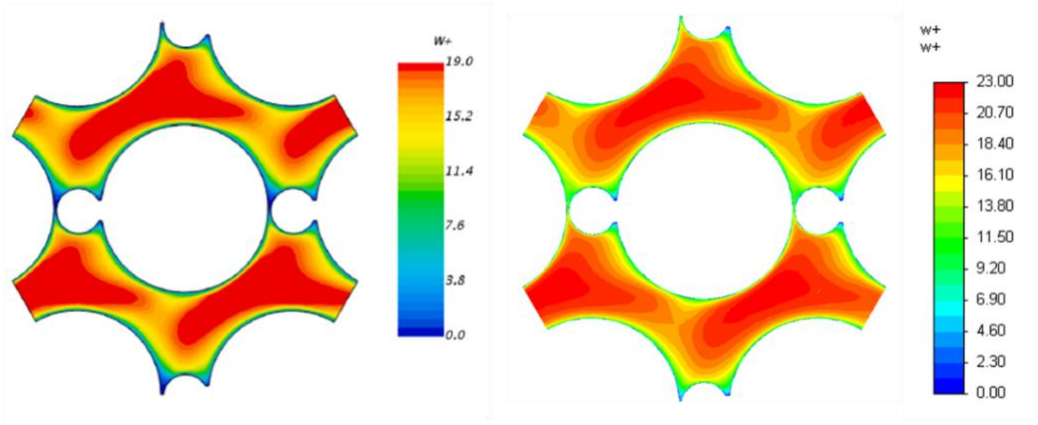

(a) W^+ , Dovizio et. al. (2019). (b) W+, author's result.

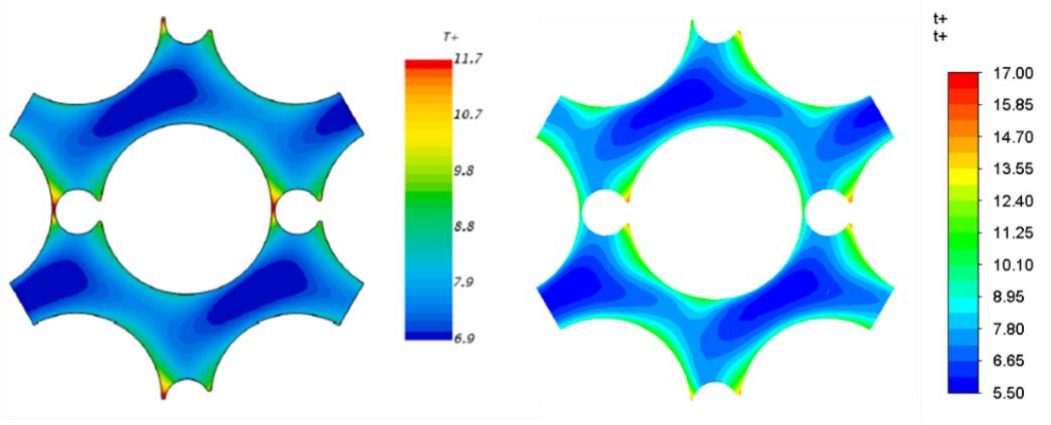

(c) T^+, Dovizio et. al. (2019). (d) T^+, author's result.

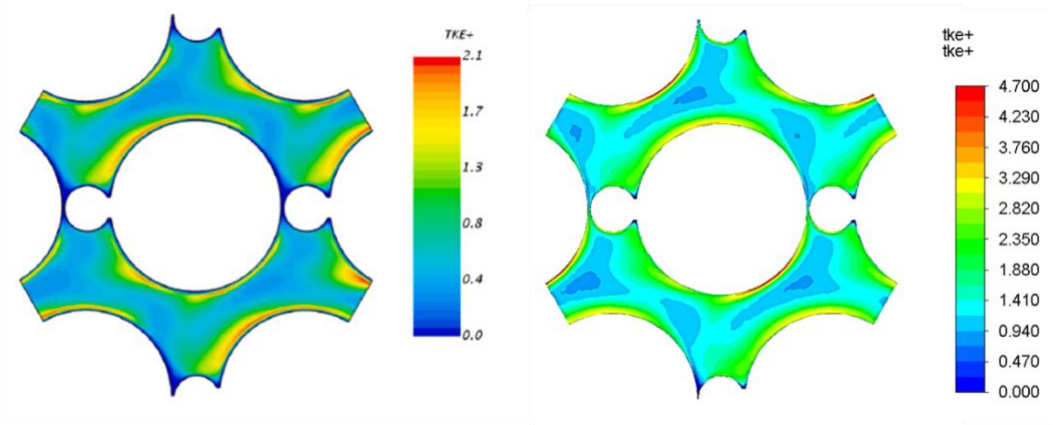

(e) TKE^+ , Dovizio et. al. (2019). (f) TKE^+, author's result.

Figure 5: *Contour comparison for W^+, T^+ and TKE^+.*
Source: Authors

3.2. Quantitative comparison with validated k-ω SST results

The following quantitative results comparisons are plotted in a Cartesian plane along the normalized axis $s^+ = s/D$, where s is the absolute position along the evaluated line (L1 to L4) and D is the central rod diameter, using the same coordinate ranges from [8]. Figure 6 to Figure 10 present the comparisons for W^+, T^+ and TKE^+.

Following to the plotted results, regions where the averaged velocity has a negative offset are the ones with higher averaged temperature values, such as between L1's $s^+ = 0.5$ and $s^+ = 0.6$ and between L2's $s^+ = 0.10$ and $s^+ = 0.12$. For the TKE^+ values, the observed positive curve offsets are directly related the W^+ offsets, as higher velocities lead to higher turbulence, given that the flow is already turbulent itself.

Again, one possible cause for the differences in the velocity fields, and all their consequences, can be explained by the inlet-outlet periodic boundary conditions, in which the mass flow rate imposed in this work is, at best, a simplified estimate of uniform conditions along the domain cross section.

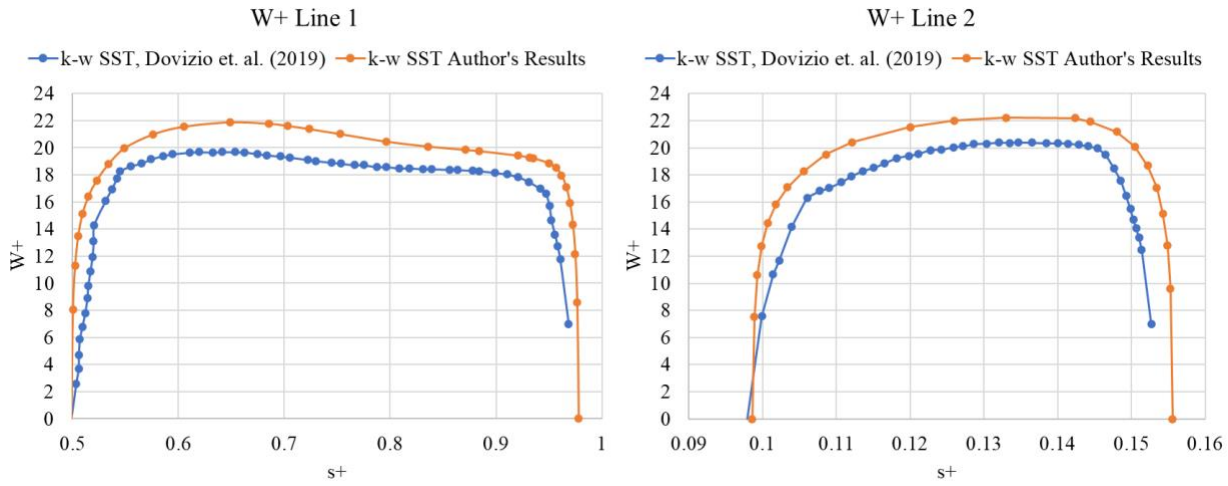

Figure 6: *Quantitative comparison results for W^+ at L1 and L2.*
Source: Authors

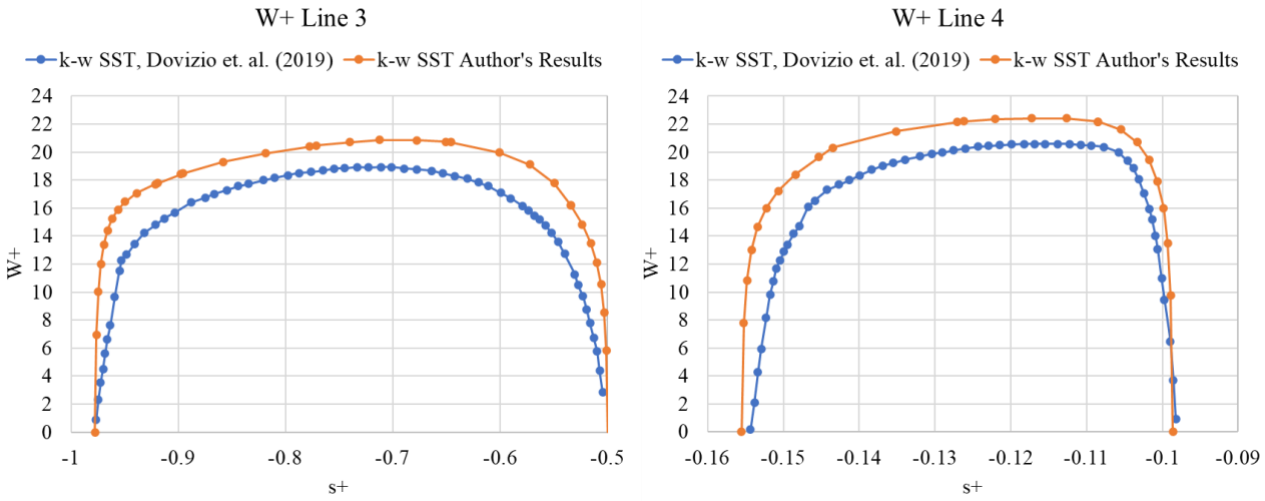

Figure 7: *Quantitative comparison results for W^+ at L3 and L4.*
Source: Authors

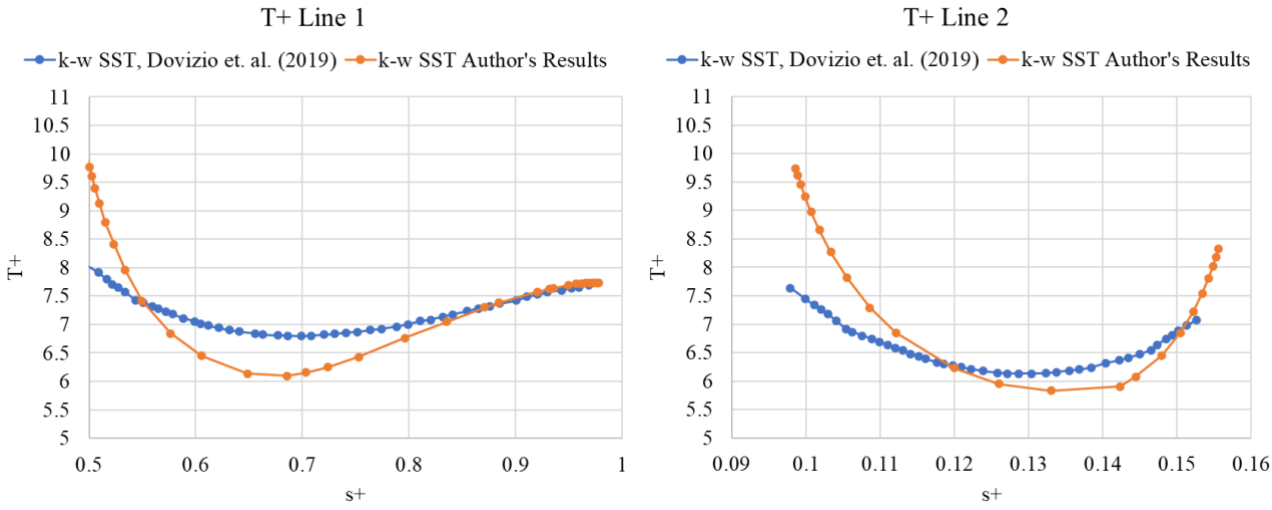

Figure 8: *Quantitative comparison results for T^+ at L1 and L2.*
Source: Authors

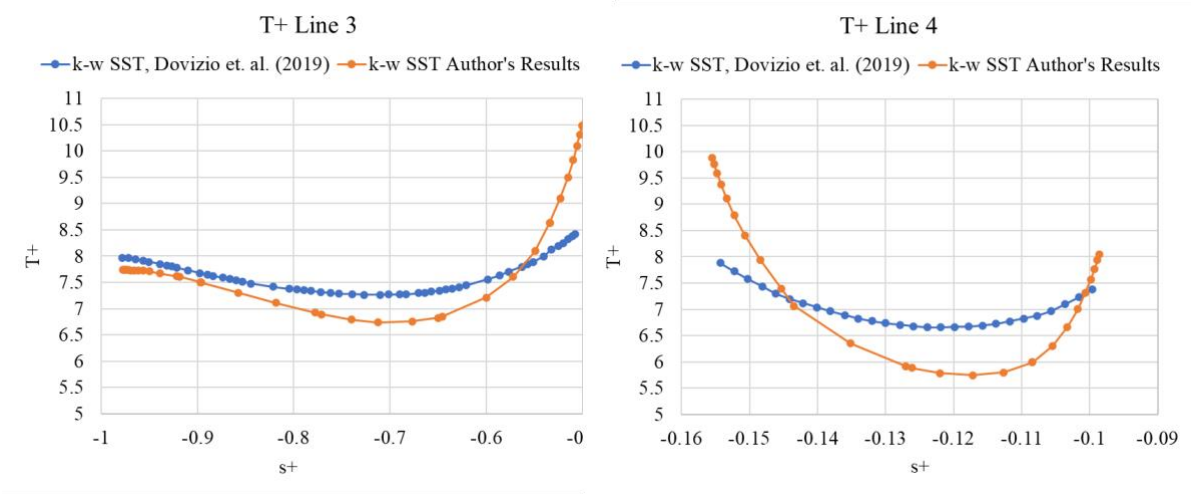

Figure 9: *Quantitative comparison results for T^+ at L3 and L4.*
Source: Authors

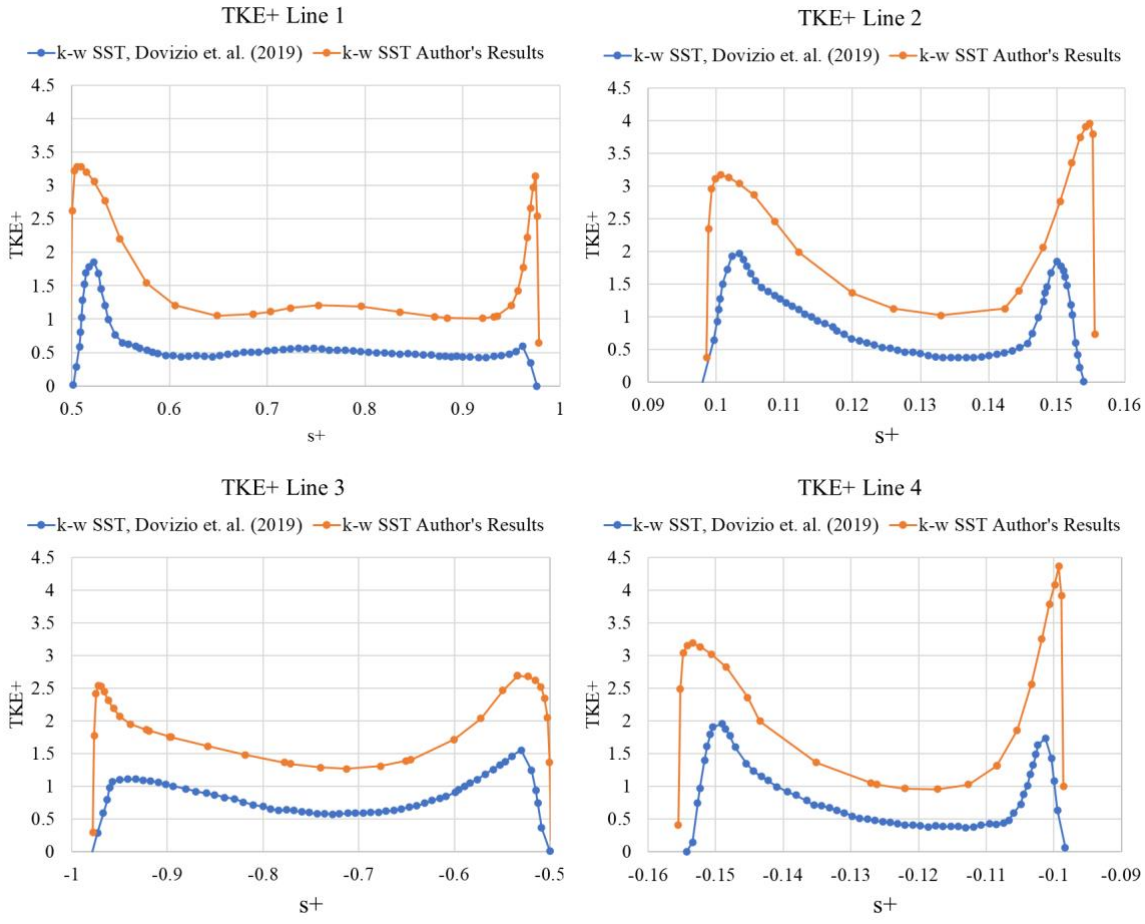

Figure 10: *Quantitative comparison results for TKE^+ at L1, L2, L3 and L4.*
Source: Authors

3.3. Influences of using temperature dependent LBE properties

Using mesh 2 and modelling the LBE coolant with constant and variable properties from Table II and Table III, respectively, one simulation was run for each case. The results presented below are for the averaged axial velocity (W^+), Figure 11, coolant temperature (T^+), Figure 12, and turbulent kinetic energy (TKE^+), Figure 13, along L1 with the relative difference on the second vertical axis. Results for other lines are not presented, since little to no difference was observed between the cases. The relative difference was calculated by dividing the absolute difference in result by the constant property result.

Analyzing the plots below, it is clear that no significant difference between the cases can be observed. However, the case using temperature dependent thermal-physical properties took around 3 times more time to converge than the case with constant properties. This increase in solving time is possibly due to the extra computational requirement for each cell in every iteration process.

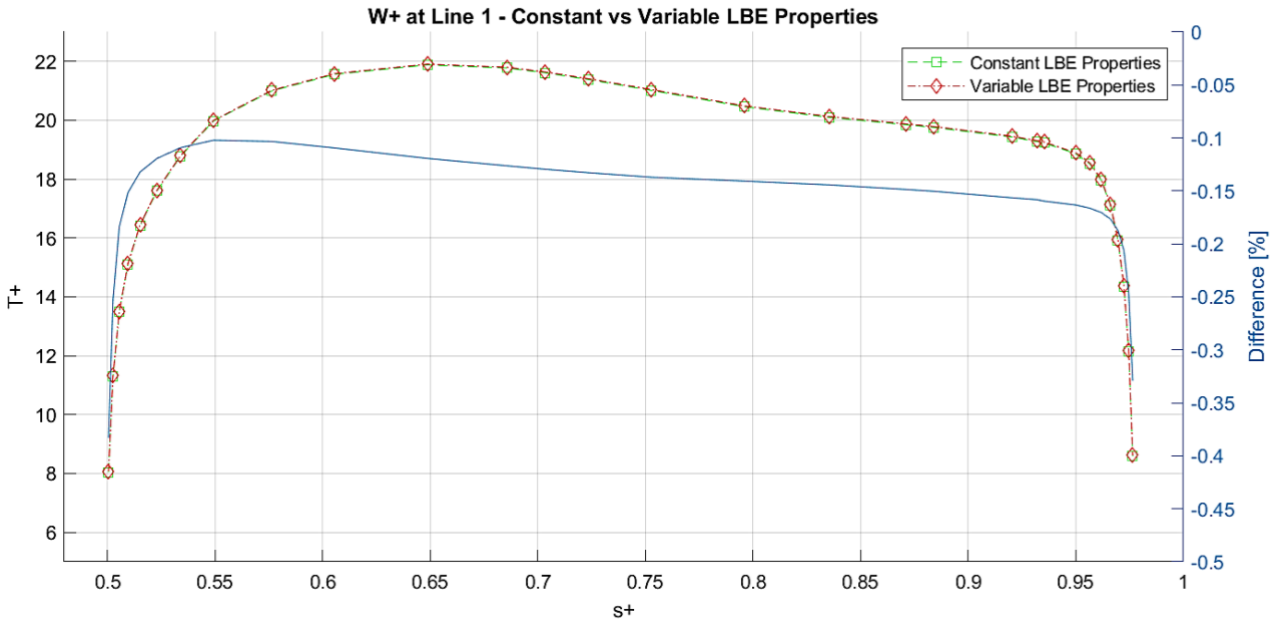

Figure 11: *Differences for W+ at L1 using constant and variable LBE properties.*
Source: Authors

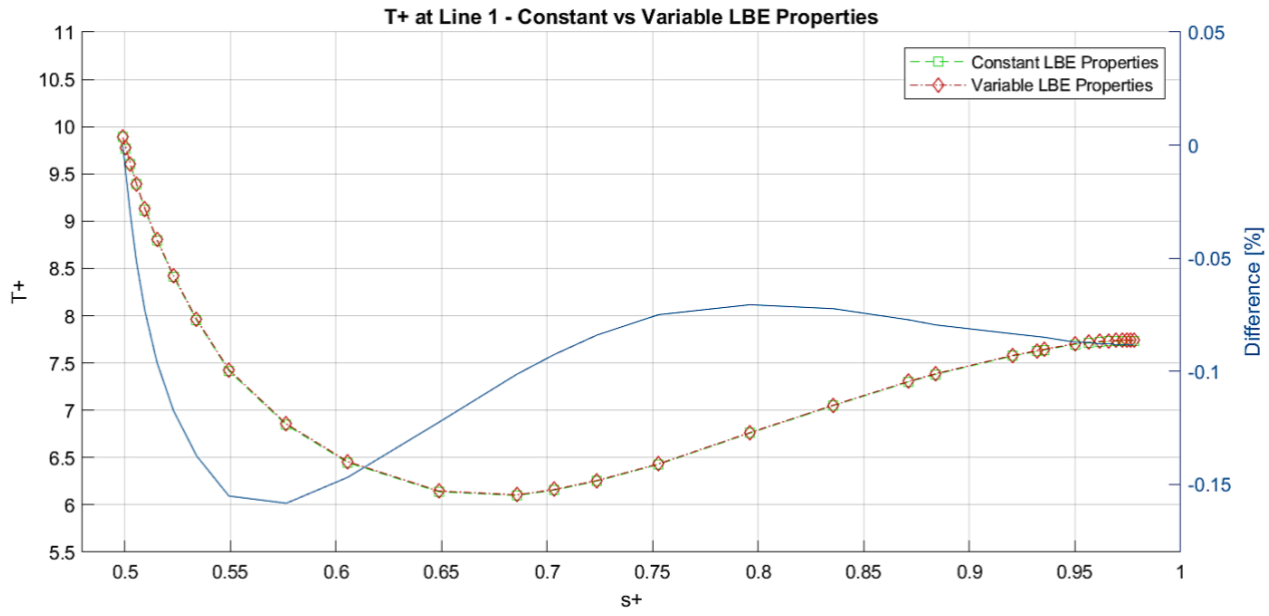

Figure 12: *Differences for T+ at L1 using constant and variable LBE properties.*
Source: Authors

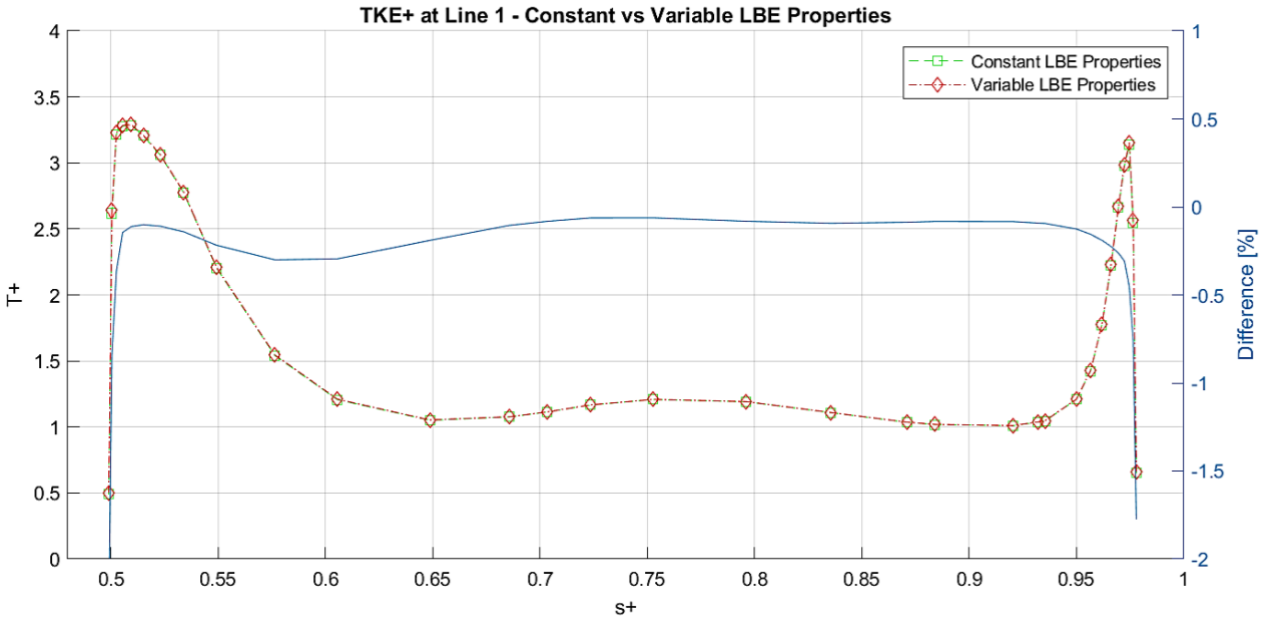

Figure 13: *Differences for TKE+ at L1 using constant and variable LBE properties.*
Source: Authors

4. CONCLUSION

This work presented a brief CFD evaluation of temperature dependent LBE properties as the coolant for an infinite wire-wrapped nuclear fuel assembly. Having as base the previous works on this geometrical domain, out of which none presented a thorough mesh sensitivity analysis, this study included this analysis using the GCI method, which demonstrated its capabilities to quantify discretization errors for this case meshes.

The comparisons to [6]'s results, using the k-ω SST turbulence model, showed that the general contours and behaviors of the coolant flow are in accordance with each other, but the numerical values themselves are not. As discussed, on possible reason for the disagreement is the lack of detailed information on the inlet-outlet periodic boundary conditions, specifically the mass flow rate used in the reference cases.

Ultimately, the comparative analysis between the results of simulations using constant and variable LBE properties indicated that no significant difference is observable, at least not in this case's the temperature range. Due to the important increase in computational time (around 300%), it is clear that the use of temperature dependent thermal physical properties is not justifiable for future similar analyses.

ACKNOWLEDGMENT

The authors are grateful to the *Coordenação de Aperfeiçoamento de Pessoal de Nível Superior* (CAPES), to *Fundação de Amparo à Pesquisa do Estado de Minas Gerais* (FAPEMIG), to *Conselho Nacional de Desenvolvimento Científico e Tecnológico* (CNPq) and to *Comissão Nacional de Energia Nuclear* (CNEN) for the support in several research projects of UFMG's Department of Nuclear Engineering.

REFERENCES

[1] GEN IV International Forum, **2020 Annual Report**, GIF, 2020.

[2] OECD-NEA, **Handbook on Lead-Bismuth Eutectic Alloy and Lead Properties, Materials Compatibility, Thermal-hydraulics and Technologies.** OECD Publishing. 2015.

[3] DE BRUYN, D.; ABDERRAHIM, H.; BAETEN, P.; FERNANDEZ, R.; VAN DEN EYNDE. G. Recent design developments of the MYRRHA ADS project in Belgium. **Proceedings of ICAPP**, p. 14-18, 2013.

[4] PACIO, J.; WETZEL, T.; DOOLAARD, H.; ROELOFS, F.; VAN TICHELEN, K. Thermal-hydraulic study of the LBE-cooled fuel assembly in the MYRRHA reactor: Experiments and simulations. **Nuclear Engineering and Design**, v. 312, p. 327–337, 2017.

[5] SHAMS, A.; ROELOFS, F.; KOMEN, E. M. J.; BAGLIETTO, E. High fidelity numerical simulations of an infinite wire-wrapped fuel assembly**. Nuclear Engineering and Design**, v. 335, p. 441–459, 2018.

[6] DOVIZIO, D.; SHAMS, A.; ROELOFS, F. Numerical prediction of flow and heat transfer in an infinite wire-wrapped fuel assembly. **Nuclear Engineering and Design**, v. 349, p. 193–205, 2019.

[7] LI, J.; FANG, D.; GUO, C.; WANG, M.; DENG, J.; TIAN, W.; QIU, S.; SU, G. H. Numerical Study on the Thermal Hydraulic Characteristics in a Wire-Wrapped Assembly of LFRs. **Frontiers in Energy Research**, v. 8, p. 1–18, 2020.

[8] SHAMS, A.; ROELOFS, F.; KOMEN, E. High-fidelity numerical simulation of the flow through an infinite wire-wrapped fuel assembly**. Int. Top. Meet. Nucl. React. Therm. Hydraul. 2015**, NURETH 2015, v. 4, p. 2817–2829, 2015.

[9] CELIK I. B.; GHIA, U.; ROACHE, P. J.; FREITAS, C. J.; COLEMAN, H.; RAAD, P. E. Procedure for estimation and reporting of uncertainty due to discretization in CFD applications, **J. Fluids Eng. Trans**. ASME, v. 130, no. 7, p. 0780011–0780014, 2008.

[10] MATHUR, A.; DOOLAARD, H.; ROELOFS, F. Reduced RANS approach validation to model passive heat removal due to inter-wrapper flow**. Nuclear Engineering and Design**. v. 353, 110278, 2019.

[11] JOSHI J.B.; NAYAK, A.K. **Advances of Computational Fluid Dynamics in Nuclear Reactor Design and Safety Assessment**. Woodhead Publishing Series in Energy. 2019.